BIOENGINEERING

Programmable and contractile materials through cell encapsulation in fibrous hydrogel assemblies

Matthew D. Davidson[1,2], Margaret E. Prendergast[1], Ehsan Ban[2,3], Karen L. Xu[1], Gabriel Mickel[1], Patricia Mensah[1], Abhishek Dhand[1], Paul A. Janmey[2,4], Vivek B. Shenoy[2,3], Jason A. Burdick[1,2]*

The natural extracellular matrix (ECM) within tissues is physically contracted and remodeled by cells, allowing the collective shaping of functional tissue architectures. Synthetic materials that facilitate self-assembly similar to natural ECM are needed for cell culture, tissue engineering, and in vitro models of development and disease. To address this need, we develop fibrous hydrogel assemblies that are stabilized with photocrosslinking and display fiber density–dependent strain-responsive properties (strain stiffening and alignment). Encapsulated mesenchymal stromal cells locally contract low fiber density assemblies, resulting in macroscopic volumetric changes with increased cell densities and moduli. Because of properties such as shear-thinning and self-healing, assemblies can be processed into microtissues with aligned ECM deposition or through extrusion bioprinting and photopatterning to fabricate constructs with programmed shape changes due to cell contraction. These materials provide a synthetic approach to mimic features of natural ECM, which can now be processed for applications in biofabrication and tissue engineering.

INTRODUCTION

Natural fibrous matrices, such as fibrin and collagen, are components of the extracellular matrix (ECM) and are widely used in vitro for applications such as gel contraction assays in mechanobiology (*1*), self-assembly of vasculature (*2*) and microtissues (*3*), and emerging biofabrication and tissue engineering techniques (*4*–*6*). The use of ECM-derived materials is motivated by their inherent bioactivity and ability to integrate with, rather than restrict, cellular processes (*7*). For example, cell contractility is responsible for many self-assembly or morphogenic processes in vivo, such as shaping tissues in embryonic development (*8*) and closing wounds during healing (*9*). Tissue contraction is mediated by the collective action of cells linked together through a web-like network of fibrous ECM molecules, such as collagen and fibrin. Fibrous ECM has structural (e.g., subcellular-scale fiber diameters and micrometer-scale porosity) (*10*) and mechanical properties (e.g., strain-stiffening behavior) (*11*) that support cell contraction and mechanical interactions between cells through the matrix (*12*).

Although useful in many applications, natural matrices have stringent conditions for assembly and may be difficult to control with respect to biochemical and biophysical properties, which limits their reproducibility and utility in many applications (*7*). Furthermore, other ECM-derived matrices, such as Matrigel and decellularized ECM, are widely used in cell culture, in tissue engineering, and even as clinical therapies; however, their batch variability and animal sourcing are limiting (*13*). As an alternative, tunable synthetic materials that closely mimic ECM properties and facilitate self-assembly processes offer a high level of control for the development of tissues in vitro and the study of cell-ECM interactions.

Numerous fibrous materials have been engineered to mimic the structure of natural ECM, including self-assembled peptides, electrospun scaffolds, and large-scale fibers. Self-assembled nanofibrous gels recapitulate the structure and scale of ECM fibrils, the smaller precursor to fibers, found in various tissues (*14*). For example, synthetic amphipathic monomers self-assemble into semiflexible filaments with diameters and persistence lengths similar to cytoskeletal polymers, and form networks with similar strain-stiffening rheology (*15*, *16*). These materials can also be coupled with cell adhesion peptides and have been used for cell culture. Although these gels permit cell encapsulation, their nanoscale porosity limits cell mobility and it is unclear whether cells can contract these materials similar to natural ECM (*14*). Micro- to nanoscale fibrous materials that permit cell encapsulation and have diameters within the range of ECM fibers (*14*) have also been described; however, the materials used in these systems are highly rigid, providing fibers that cells cannot physically remodel (*17*). Another important material is formed by electrospinning hydrogel fibers with moduli similar to natural ECM that allow cells to contract and compact fibers in a manner similar to collagen contraction (*18*); however, these electrospun scaffolds are rather stiff preformed porous solids that are not amenable to cell encapsulation or extrusion bioprinting. Last, supracellular scale synthetic fibrous (*19*) or ribbon-like (*20*) materials that permit cell encapsulation and approximate the size of large collagen fibers (*14*) have also been described; however, their large sizes hinder multicellular interactions through the matrix. Thus, synthetic systems with improved control over structure and mechanics would provide the field with tools to study cell-ECM interactions and engineer self-assembled tissues through combined top-down and bottom-up approaches.

To overcome the limitations of current engineered systems, we report here on fibrous hydrogel assemblies composed of micro- to nanodiameter fibers that are fabricated from diverse materials, are injectable, and exhibit strain-stiffening behavior based on fiber density. In addition, this system permits cell encapsulation and contractility, features that allow assembly into microtissues and the fabrication of cell-laden constructs. These materials are programmable by altering

[1]Department of Bioengineering, University of Pennsylvania, Philadelphia, PA 19104, USA. [2]Center for Engineering Mechanobiology, University of Pennsylvania, Philadelphia, PA 19104, USA. [3]Department of Materials Science and Engineering, University of Pennsylvania, Philadelphia, PA 19104, USA. [4]Institute for Medicine and Engineering, University of Pennsylvania, Philadelphia, PA 19104, USA.
*Corresponding author. Email: burdick2@seas.upenn.edu

the extent of contractility through fiber density, the shape of constructs through patterning, and dynamic shape changes with culture through the fabrication of multimaterial constructs.

RESULTS

Generation of photocrosslinkable fibrous hydrogel assemblies

To recreate the three-dimensional (3D) architecture of fibrous ECM, we introduce a method to fabricate suspensions of hydrogel fibers that can be assembled and crosslinked into a highly porous fibrous network (Fig. 1A). This process involves (i) mechanical fragmentation of electrospun hydrogel fiber mats into fiber suspensions, (ii) assembly of fibers into networks through fiber concentration at desired densities, and (iii) stabilization of fiber networks through photocrosslinking to form fibrous hydrogel assemblies.

The fragmentation process is a simple approach to fabricate fiber suspensions from electrospun scaffolds, primarily in this study with norbornene-modified hyaluronic acid (NorHA) (fig. S1). This builds on recently described methods to generate segments of hydrogel fibers using photopatterned crosslinking (*21*) and mechanical disruption (*22*). NorHA has been routinely processed into fibrous hydrogel scaffolds through electrospinning, using thiol-ene reactions to stabilize scaffolds with both interfiber and intrafiber crosslinking (*23*). Electrospun scaffolds are limited in that they are not injectable and cannot be used to encapsulate cells; however, fragmentation converts these scaffolds into hydrogel fiber suspensions that overcome these limitations. Specifically, electrospun scaffolds are cut into small pieces, briefly hydrated, passed repeatedly through a syringe needle, and purified from any larger fragments with filtration, which disrupts interfiber crosslinks and fractures fibers along their length (fig. S2 and movie S1). There are many parameters that can be varied in the

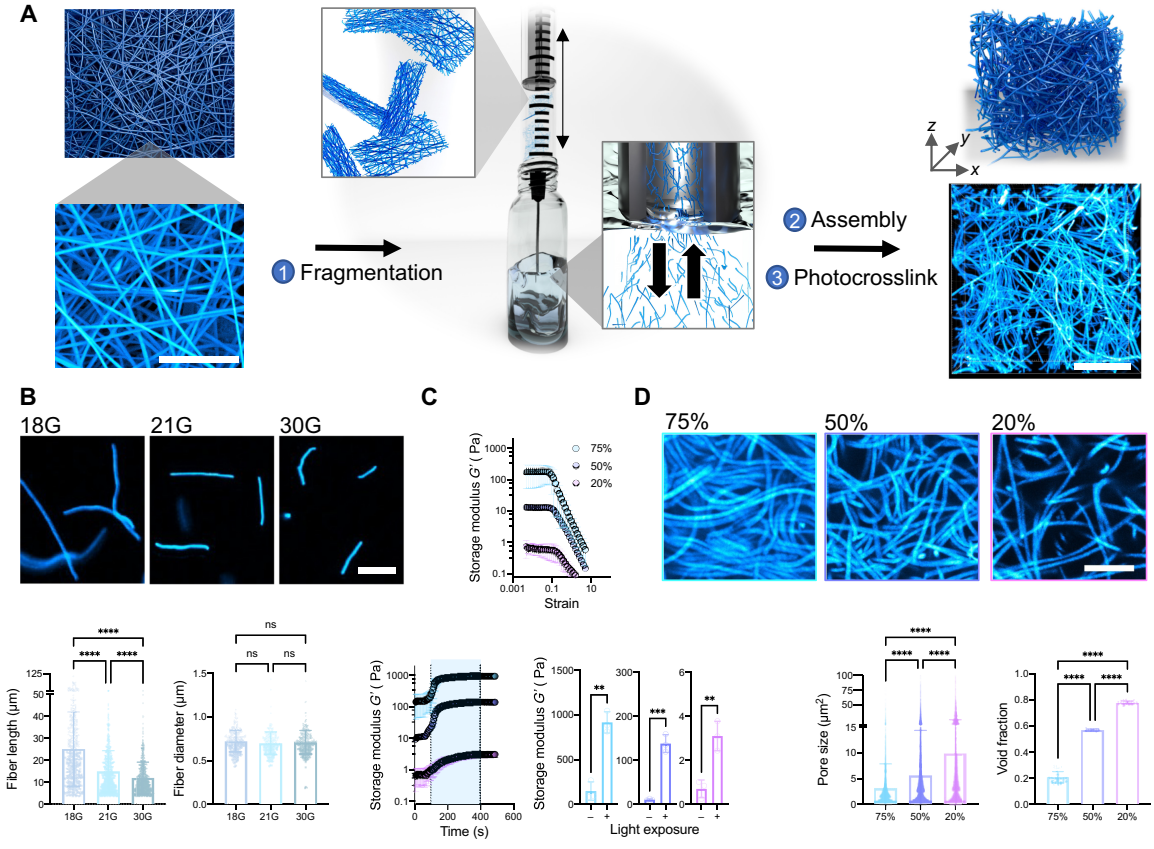

Fig. 1. Fabrication of fibrous hydrogel assemblies. (**A**) Schematics (left top, center, and right top), as well as scanning electron microscopy (left bottom) and fluorescent (right bottom) images demonstrating (1) the production of fiber suspensions from electrospun scaffolds via fragmentation by passing scaffold pieces repeatedly through a syringe needle, (2) assembly of fibers into a fibrous network, and (3) photocrosslinking of the fibrous network for stabilization through interfiber crosslinking. Images are representative of $n = 3$ independent samples. Scale bars, 5 μm (left) and 25 μm (right). (**B**) Representative fluorescent images (top) and quantification of fiber length (bottom left) and diameter (bottom right) for NorHA fiber suspensions obtained from fragmentation with 18-gauge (18G), 21-gauge (21G), or 30-gauge (30G) needles. Images and data are representative of $n = 3$ independent experiments [fiber length, mean ± SD, one-way analysis of variance (ANOVA), 18-gauge versus 21-gauge $P = 1.0 \times 10^{-15}$, 18-gauge versus 30-gauge $P = 1.0 \times 10^{-15}$, 21-gauge versus 30-gauge $P = 5.0 \times 10^{-7}$]. Scale bar, 25 μm. (**C**) Storage modulus (G') of assemblies before photocrosslinking with increasing strain (top), during photocrosslinking (bottom left, blue region denotes visible light exposure at 5 mW/cm^2), and after photocrosslinking (bottom right) at varied fiber densities (75, 50, and 20%) (mean ± SD, $n = 3$ independent samples). (**D**) Representative fluorescent images (top) and quantification of pore size (in μm^2) (bottom left) and void fraction (bottom right) of assemblies at varied fiber densities (75, 50, and 20%). Images and data are representative of $n = 3$ independent samples (pore size, mean ± SD, one-way ANOVA, 18-gauge versus 21-gauge $P = 1.0 \times 10^{-7}$, 18-gauge versus 30-gauge $P = 1.0 \times 10^{-7}$, 21-gauge versus 30-gauge $P = 5.0 \times 10^{-7}$; void fraction, mean ± SD, one-way ANOVA, 18-gauge versus 21-gauge $P = 2.0 \times 10^{-11}$, 18-gauge versus 30-gauge $P = 2.0 \times 10^{-11}$, 21-gauge versus 30-gauge $P = 2.0 \times 10^{-11}$). Scale bar, 10 μm (ns, not significant; $^{**}P < 0.01$, $^{***}P < 0.001$.

fragmentation process and electrospun scaffold properties to influence final fiber lengths, such as the needle gauge used to fragment fibers, extent of crosslinking of the fibers, and fragmentation speed. We observe that increased needle gauge, increased fragmentation speed, and reduced crosslinking result in fibers with decreased lengths but maintained fiber diameters (Fig. 1B and figs. S3 and S4). Variance in fiber lengths is reduced by increasing the number of fragmentation steps and speed of fragmentation [20 fast fragmentation steps [coefficient of variation (CV): 70.8%], 40 slow fragmentation steps (CV: 98.5%), and 40 fast fragmentation steps (CV: 65.7%)]. Furthermore, the fragmentation process is reproducible across multiple users and is compatible with electrospun scaffolds from a wide range of polymers [e.g., gelatin (NorGel, GelMA), poly(ethylene glycol) (NorPEG), and HA (MeHA)], which illustrates the versatility of the fragmentation technique (figs. S4 and S5).

To improve upon fiber yield, we implement a multifiber electrospinning process, where sacrificial fibers of a dissolvable poly(ethylene oxide) (PEO) are electrospun with stable NorHA fibers (fig. S6). The sacrificial fiber population physically blocks interfiber bonds during scaffold fabrication but then dissolves away, allowing easier fragmentation (*24*). Overall, this process results in reproducible NorHA fibers with lengths similar to those reported for natural ECM [~7 to 23 μm for NorHA fibers versus ~3.6 to 21.9 μm for collagen gel fibers (*25*)] and ECM-like fiber diameters (*14*) [~700 nm for NorHA fibers versus ~310 to 899 nm reported for type I collagen gel fibers (*25*), or ~350 nm for collagen I in this study] (Fig. 1B and figs. S6 and S7). Fiber diameter changes with collagen concentration or polymerization parameters, but is consistent across different fiber assembly densities in our approach, highlighting a unique advantage with our material system for controlled cell-ECM interaction studies. The remaining studies carried out with NorHA fibers (~50% consumption of norbornene groups based on calculated level of norbornene modification) were fabricated using the multifiber electrospinning approach and multiple fragmentation steps (18-gauge, then 21-gauge needle, with 40 passes through each needle) to achieve fibers with an average length of ~11 μm. This approach provides a rapid and efficient method to generate fiber suspensions and overcomes challenges with alternate approaches, such as issues with light diffusion and polymer loss using photopatterning (*21*), lengthy multistep protocols for cryosectioning (*26*), or harsh chemical treatments with aminolysis (*27*).

After production, fiber suspensions are centrifuged and resuspended at desired concentrations (75, 50, and 20%, v/v) to form fiber assemblies. These assemblies behave as yield stress fluids at all fiber densities investigated, showing yielding behavior with increased strain (Fig. 1C). In addition, the assemblies are injectable and exhibit shear-thinning and self-healing behavior, represented as a reduction in viscosity with increasing shear rate and a loss and recovery of storage moduli across cycles of low and high strains, likely due to loss of fiber entanglement with the application of external force and reestablishment of entanglement upon removal of external forces (fig. S8). After assembly, remaining norbornene groups on the fibers can be used for an additional thiol-ene reaction to stabilize the networks. This overcomes an unavoidable issue with low-concentration natural fibrous ECMs, where gels must be polymerized after injection to avoid damaging fiber networks during extrusion, while fiber assembly networks can be assembled, injected, and then reassembled before crosslinking. Specifically, additional photoinitiator [lithium phenyl-2,4,6-trimethylbenzoylphosphinate (LAP)] and crosslinker (4-arm PEG-thiol, 5 kDa) are added to the assemblies, which then photocrosslink with exposure to visible light (400 to 500 nm λ), measured as an increase in storage modulus (G') (75%: 146.4 to 915.6 Pa, 50%: 10.5 to 138.2 Pa, and 20%: 0.7 to 3.1 Pa) (Fig. 1C). These final moduli are within the range of type I collagen gels polymerized at 37°C with variable collagen concentrations (6 mg/ml: 1113 Pa, 2.5 mg/ml: 209 Pa, and 1 mg/ml: 7.6 Pa) (fig. S7).

To enable visualization of fibers, fluorescent dextran is included in the electrospinning process; however, the addition of dextran does not affect the mechanical properties of fiber assemblies (fig. S9). Fiber assemblies made with longer fibers at the same concentration (20%, v/v) have lower storage moduli after photocrosslinking (fig. S10). Although other chemistries could be used to introduce interfiber bonds, such as physical crosslinks or dynamic covalent chemistry (*23*), the norbornene chemistry and thiol-ene reaction results in covalently crosslinked stable networks. Accordingly, GelMA fiber assemblies fabricated with free-radical polymerization are stable at a 50% fiber density, showcasing the versatility of this approach for other chemistries and polymer backbones (fig. S11). NorHA-based fibrous hydrogel assemblies, referred to as fibrous assemblies from here onward, have pore sizes (~3 to 10 μm^2 for assemblies versus 1.4 to 6.8 μm^2 for type I collagen gels) and void fractions (~21 to 78% for assemblies versus ~9 to 86% for type I collagen gels based on initial fiber or collagen concentration) within the range of fibrous ECM (fig. S7) (*14*, *28*). There is notable variability in the pore size of fiber assemblies as well as type I collagen gels, and this is likely due to artifacts from imaging analysis as well as heterogeneity in the initial fiber population and collagen solutions. Reducing fiber length heterogeneity through increased fragmentation force could improve pore size variation in future studies.

Strain-responsive properties and modeling of fibrous hydrogel assemblies

Cells physically strain and compact fibrous ECM during tissue contraction, motivating the introduction of strain-responsive properties into engineered fibrous assemblies. The micrometer-scale pore size of ECM is thought to contribute to their force-responsive properties, where strain causes fibers to stretch and buckle in the direction where stresses are compressive, leading to fiber alignment in the direction of strain and nonlinear stiffening (*10*, *11*). Using rheological shear strain sweeps, we observe that fibrous assemblies exhibit nonlinear mechanical properties, undergoing strain-induced increases in G' (i.e., strain stiffening) after reaching a critical strain (γ_c) (Fig. 2A), similarly to type I collagen gels (fig. S7). This is particularly pronounced with the lowest fiber density formulation of 20% volume fraction, which results in the highest relative increase in stiffness (2.3-fold) before failure, whereas the 50 and 75% volume fractions exhibit a lower increase in stiffness (~1.6- and 1.3-fold, respectively) (Fig. 2A). Collagen gels display similar behavior, with lower concentration gels exhibiting higher relative increases in moduli; however, the relative increases in collagen moduli are higher than what is observed with fiber assemblies (~8.5-fold for 1 mg/ml gels), but still within the same magnitude. This is likely due to differences in the pore size to fiber diameter ratio, as fiber assemblies have larger fiber diameters than collagen. The critical strains (γ_c) of fibrous assemblies (~4 to 6% strain) are similar to those measured with natural fibrous ECM and are within the range of strains that cells impose on the ECM (maximum of ~30 to 50% strain), suggesting that cellular strains could potentially stiffen these materials (*29*).

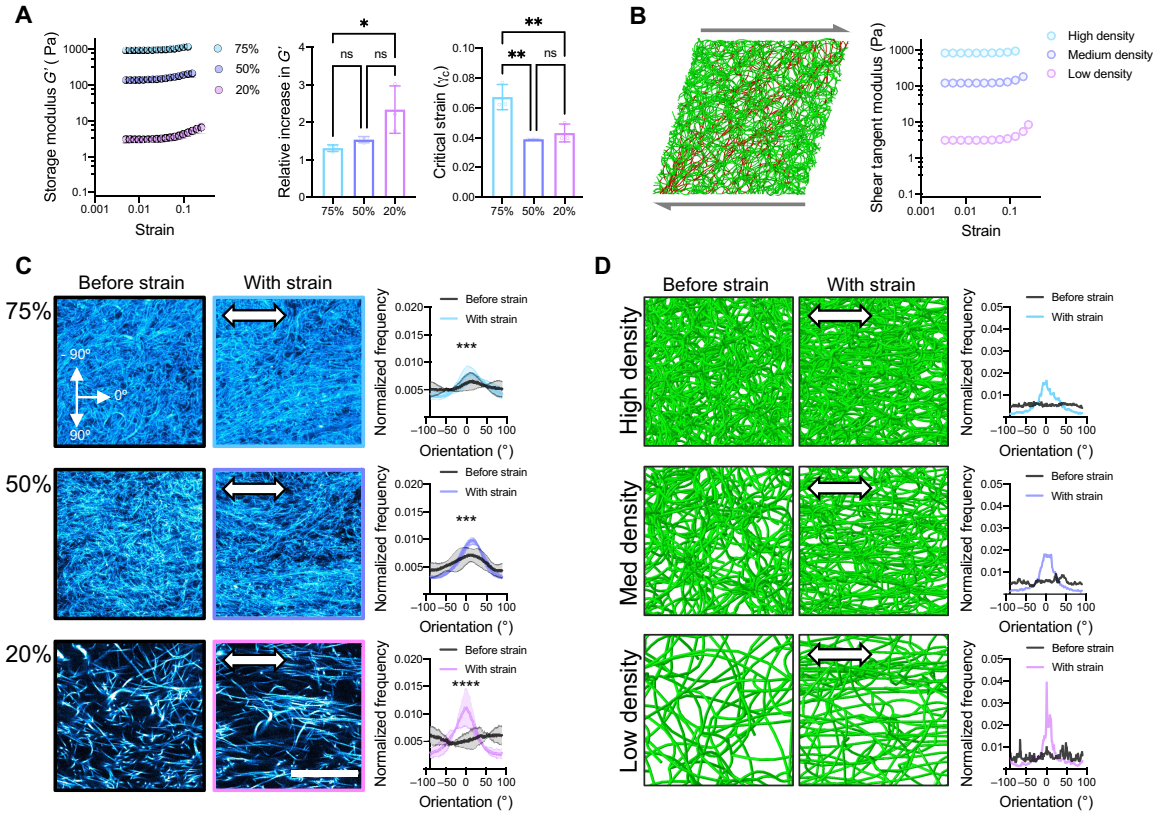

Fig. 2. Strain-responsive behavior of fibrous hydrogel assemblies. (**A**) Storage modulus (G') with increasing strain (left, 0.005 to 0.5 strain, 1 Hz), relative increase in G' before failure (center, normalized to modulus at low strain, 0.01), and critical strain (γ_c, onset of stiffening) of NorHA assemblies at varied fiber densities (75, 50, and 20%) ($n = 3$ gel samples, mean ± SD, one-way ANOVA; relative increase in G', 75% versus 20% $P = 0.034$; γ_c, 75% versus 50% $P = 0.003$, 75% versus 20% $P = 0.006$). (**B**) Snapshot of discrete fiber network model deforming under shear strain (left, red fibers indicate stretched fibers) and model tangent modulus with increased shear strain (right, 0.05 to 0.5 strain) at varied network densities (high, medium, and low). (**C**) Representative fluorescent images [before (left column) and with uniaxial strain (center column, ~0.1 strain)] and quantification of NorHA fiber orientation (right column) within assemblies before and with strain at varied fiber densities (75, 50, and 20%) ($n = 3$ samples, mean ± SD, Watson-Wheeler test for homogeneity, 75% $P = 0.0005$, 50% $P = 0.0005$, 20% $P = 7.0 \times 10^{-6}$). Scale bar, 25 μm. (**D**) Representative snapshots of fiber network model before (left column) and with simulated uniaxial strain (center column) and profiles of fiber orientation (right column) in model networks before and with strain at varied fiber densities (high, medium, and low) (*$P < 0.05$, **$P < 0.01$, ***$P < 0.001$, and ****$P < 0.0001$).

To further understand the influence of fiber density on strain stiffening, we introduce a discrete fiber network computational model based on the structure and mechanics of fibrous assemblies and imposed shear strains on the networks (Fig. 2B). The fiber network model shows similar trends to our experimental data, with low-density fiber networks exhibiting higher relative strain stiffening when compared to high-density fiber networks, and similar increases in moduli before failure. During shear tests with the fiber network model, we observe higher levels of fiber bending and reorientation with low-density networks, suggesting that fibers reorient within fibrous assemblies during strain. To investigate how imposed strains change fibrous assembly microarchitecture, we use confocal microscopy to image fiber network architectures before and during uniaxial strain (10%) (Fig. 2C and fig. S12). Fibrous assemblies undergo strain-induced alignment, with low fiber densities (20%) having the highest relative increase in alignment, whereas higher fiber densities (50 and 75%) have similar levels of alignment relative to networks that are not strained (Fig. 2C). When uniaxial strains (40% strain) are imposed on the discrete fiber network model, high levels of fiber realignment are observed in the direction of strain, with the greatest alignment observed for low-density networks (Fig. 2D).

Our engineered fiber assemblies are unique in their ability to mimic feature sizes and architecture of reconstituted fibrous ECM while also introducing parameters of injectability and tunable nonlinear properties. While other nonlinear synthetic material systems have been described (*15*, *16*, *30*), these materials fail to capture the micrometer-scale porosities, fiber diameters, lengths, and 3D architectures that we observe with these fibrous hydrogel assemblies. These results are successfully modeled to describe our experimental observations of strain stiffening and fiber alignment with variations in fiber concentration. Our results are also similar to what has been reported for type I collagen gels produced with low and high collagen concentrations (*31*), are consistent with previous computational models (*12*, *28*), and further validate the ECM-like properties of our fibrous assemblies.

Cell-mediated fiber recruitment and contractility of fibrous hydrogel assemblies

Having demonstrated that fibrous assemblies adapt to forces similar to native ECM, we next explore the interface between cells and fibers when encapsulated within fibrous assemblies, including features such as cell-mediated fiber contraction and recruitment. A major advantage

of these fibrous assemblies over existing electrospun hydrogel scaffolds is that cells can be encapsulated within the assemblies by mixing with fiber suspensions at desired fiber densities and then photocrosslinking (Fig. 3 and fig. S13). Alternative fiber systems that allow cell encapsulation exist, but they use rigid polymers that cells cannot remodel (*17*), are composites with extensible fibers embedded in a continuous gel phase that limits fiber recruitment (*21*), or are on scales that are much larger than single cells (*19*, *20*). To engage cell adhesion through integrins, fibrous assemblies are decorated with a peptide containing the adhesive RGD motif for all cell studies. Human mesenchymal stromal cells (MSCs), a prototypical cell type used in mechanobiological studies and of great interest in tissue engineering, are encapsulated within fibrous assemblies of three different fiber densities (75, 50, and 20%), and fiber recruitment and cell morphology are assessed during culture (Fig. 3).

MSCs spread and recruit fibers to the cell surface dynamically over 3 days in culture in low fiber densities (20%), whereas fiber recruitment is less apparent in higher fiber densities (Fig. 3B). At high fiber densities, there are likely impediments to fiber recruitment due to the high fiber concentrations and resulting greater mechanical resistance. Although differences in cell morphology are observed after 1 day of culture, there are no statistically significant differences in cell aspect ratio and circularity across the three fiber volume fractions after 3 days in culture, suggesting that cells are able to spread within all fibrous assemblies, regardless of initial conditions. These cellular observations can be compared to commonly used collagen gels. Cells encapsulated in collagen gels for 6 hours exhibit similar behaviors to cells within fiber assemblies after 24 hours, with cells recruiting collagen fibers to the cell membrane and displaying decreased circularity and increased aspect ratios in lower versus higher collagen concentrations (fig. S14). Low–cell density collagen studies are stopped at 6 hours because of substantial macroscopic contraction that occurs with prolonged culture at the cell densities used for fiber assembly studies (which do not contract over 3 days). Cell morphologies follow similar trends in fiber assemblies fabricated with longer fibers or GelMA fibers (figs. S15 and

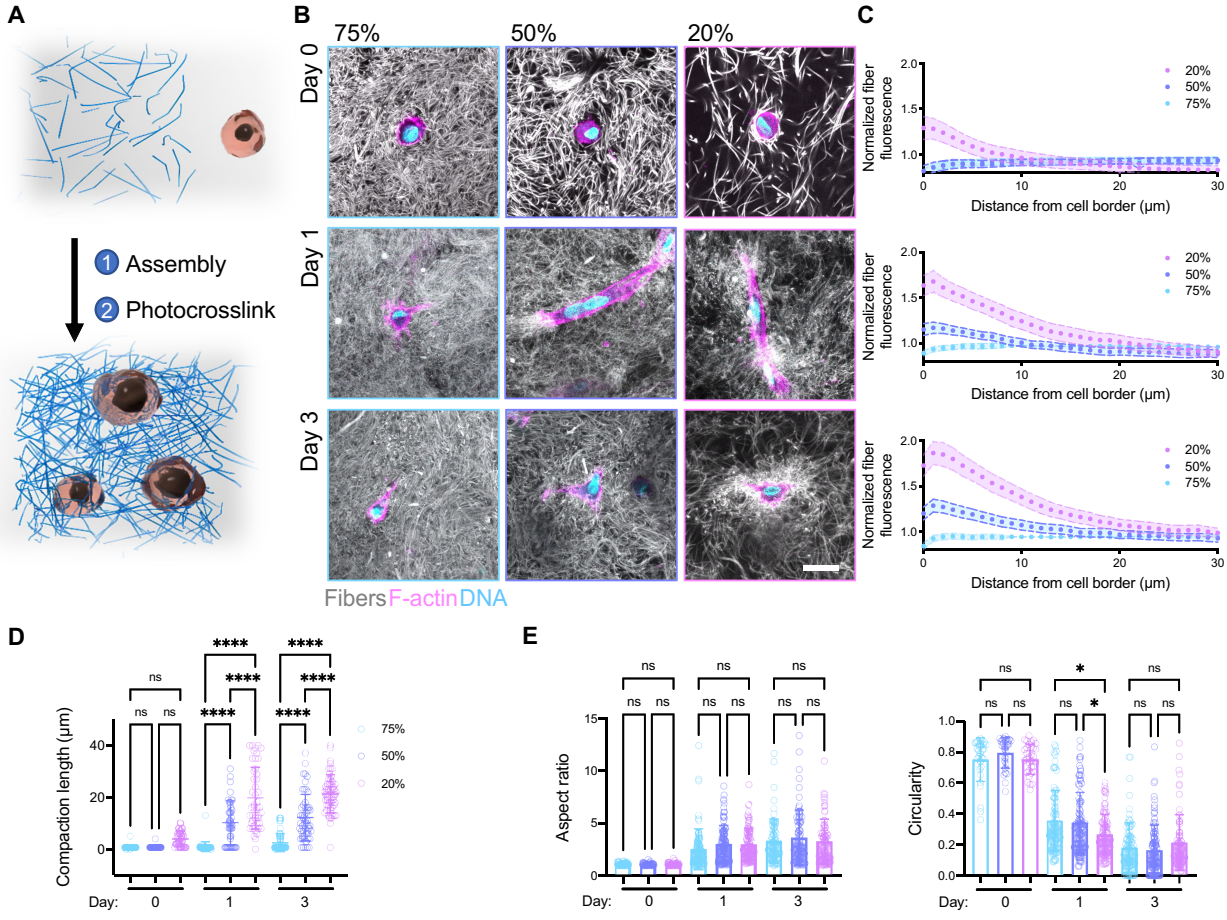

Fig. 3. MSC behavior within fibrous hydrogel assemblies. (**A**) Schematic of cell encapsulation process through fiber assembly and photocrosslinking and (**B**) representative fluorescent images of encapsulated cells [actin (pink), nuclei (blue), and NorHA fibers (gray)] at day 0 (top), day 1 (middle), and day 3 (bottom) of culture at varied fiber densities (75, 50, and 20%). (**C**) Profiles of normalized fiber fluorescence at days 0 (top), 1 (middle), and 3 (bottom) of culture (normalized to fluorescence intensity in a remote area without cells) at varied fiber densities (75, 50, and 20%) (day 0: $n = 34$, 28, and 45 cells, day 1: $n = 42$, 41, and 46 cells, day 3: $n = 53$, 54, and 52 cells for 75, 50, and 20%, respectively, mean ± SD). Quantification of (**D**) fiber compaction length (distance away from cell border where compacted fiber fluorescence intensity reaches background intensity) and (**E**) cell morphology (aspect ratio, circularity from max *z* projections of encapsulated cells) at varied fiber densities (75, 50, and 20%) on days 0, 1, and 3 of culture ($n > 25$ cells from three biologically independent experiments per condition at each time point, mean ± SD, two-way ANOVA). Scale bars, 25 μm (*$P < 0.05$ and ****$P < 0.0001$). *Statistical comparisons between time points are not shown (D and E).

S16). Cells encapsulated in nonfibrous NorHA hydrogels [3.5 weight % (wt %)] remain viable but do not spread over 3 days of culture, highlighting the importance of a fibrous network structure in promoting rapid cell spreading (fig. S17).

While cell morphology is similar across the different initial fiber densities, we observe large differences in the levels of fiber recruitment. This is quantified by measuring the average fiber fluorescence intensity in 2D radial bands around cells (using 1-μm increments) to define a fiber compaction length that can be compared to remote fiber locations (Fig. 3C and fig. S13). Cells in low fiber densities (20%) compact large fiber "shells" (19.7 and ~21.3 μm in radius for days 1 and 3, respectively) around the cell surface, while fiber compaction length decreases with medium and high fiber densities (~12- and ~2.5-μm shell radius for 50 and 75% at day 3, respectively) (Fig. 3, D and E). Similarly, cells embedded in collagen recruit fibers to the cell body and create concentration gradients of collagen around the cell that have lengths similar to the shells of fibers observed in fiber assemblies (9, 8.6, and 5.8 μm in radius for 1, 2.5, and 6 mg/ml, respectively). The rate of decay in collagen versus fiber assembly density profiles is different, with collagen showing a more nonlinear decay and fiber assemblies showing a more linear decay. These results are supported by the previous experiments and simulations with our fiber network model, which show that the smaller pores and higher elastic moduli in high-density fiber formulations limit the extent of fiber reorganization that can occur, while large pores support fiber reorganization and compaction.

Having established that cells can locally compact fibrous assemblies, we next explore whether the collective contraction of cells at higher densities results in macroscale contraction (Fig. 4A). When MSCs are encapsulated at high densities (1×10^7 cells/ml) and the gel area is monitored over time, we observe high cell viability and bulk contraction of constructs fabricated with low fiber densities (20%) within 1 day of culture (~36% of original area), while contractions are greatly reduced with increasing fiber densities (~85 and 95% of original area for 50 and 75% fiber densities, respectively) (Fig. 4, B to D, and fig. S18). Fiber assemblies fabricated with longer fibers show slightly higher levels of contraction (~25% of original area), although this is not significantly different from shorter fibers (fig. S15). After 3 days of culture, contraction stabilizes and low fiber densities (20%) decrease to ~12% of their original volume, while higher fiber densities only decrease in volume to ~51 and 78% of their original volume, for medium (50%) and high (75%) fiber densities, respectively (Fig. 4C). Contraction of GelMA fiber assemblies continues beyond 3 days of culture (from 46% of original area at day 1 of contraction down to 28% of original area at 7 days), which could be due to cell-mediated degradation of fibers or differences in biochemical ligands found on gelatin (fig. S16). Cells encapsulated in collagen gels display similar trends, with lower collagen concentrations promoting higher levels of contraction, although contraction kinetics are faster (2 hours to achieve similar contraction observed in 24 hours for fiber assemblies) and higher levels of contraction are observed (down to 17.6% of original area over 12 hours) than fiber

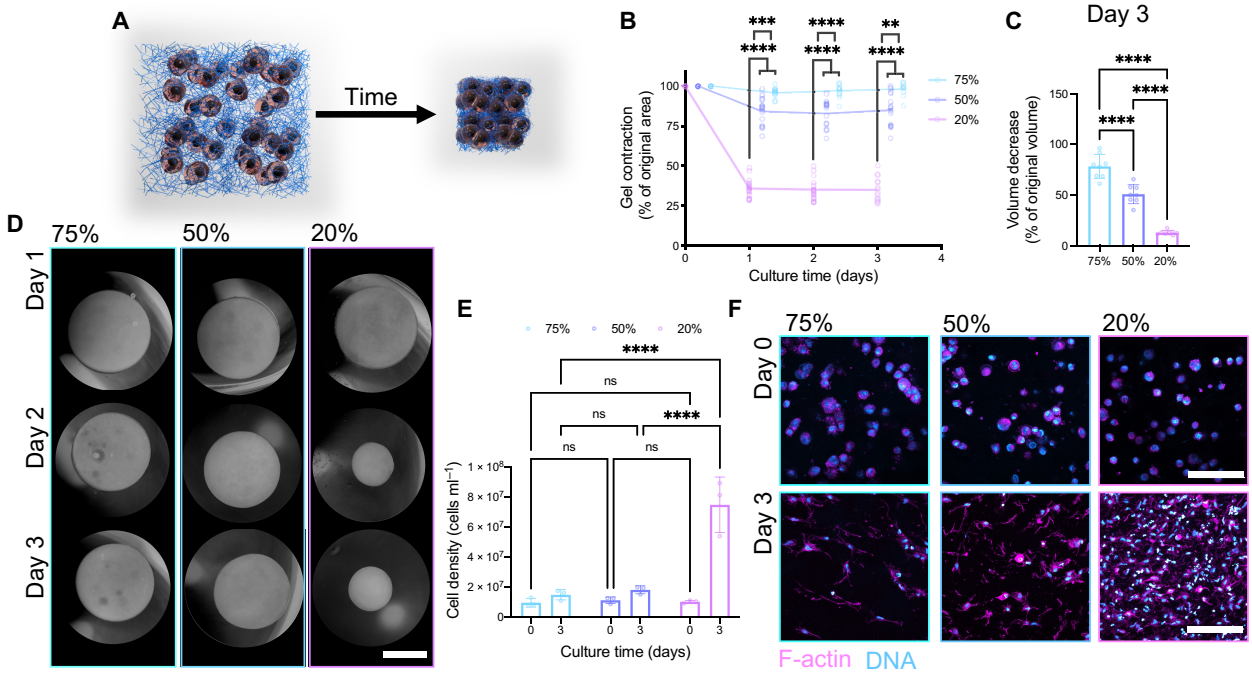

Fig. 4. Multicellular contraction of fibrous hydrogel assemblies. Schematic (**A**) and quantification (**B**) of assembly contraction (% of original sample area) over time for MSCs (1×10^7 cells/ml) encapsulated within NorHA assemblies with varied fiber densities (75, 50, and 20%) ($n > 10$ for at least three biologically independent experiments per condition at each time point, mean ± SD, two-way ANOVA). (**C**) Quantified contraction induced volume decrease at day 3 (relative to day 0 volume) for varied fiber densities (75, 50, and 20%) ($n = 8$ samples from two biologically independent experiments, mean ± SD, one-way ANOVA). (**D**) Representative inverted phase-contrast images of assemblies over time with varied fiber densities (75, 50, and 20%). Images are representative of $n = 3$ for 75% and $n = 4$ for 50 and 20% independent experiments. Scale bar, 2 mm. (**E**) Quantification of cell density and (**F**) representative fluorescent images [actin (pink) and DNA (blue)] for MSCs encapsulated within assemblies after 0 or 3 days of culture with varied fiber densities (75, 50, and 20%) ($n = 3$ biologically independent experiments, mean ± SD, two-way ANOVA). Images are representative of $n = 3$ biologically independent experiments. Scale bars, 100 μm (**$P < 0.01$, ***$P < 0.001$, ****$P < 0.0001$).

assemblies (fig. S19). Macroscopic contraction of nonfibrous NorHA hydrogels is not observed ever with high cell densities (fig. S17). As gel volume decreases, the cell density simultaneously increases more than sevenfold to 7.1×10^7 cells/ml for low fiber densities (20%), whereas the cell density only slightly increases to 1.8×10^7 and 1.5×10^7 cells/ml for medium (50%) and high (75%) fiber densities, respectively (Fig. 4E). In addition, even higher cell densities are obtained after contraction (11.5×10^7 cells/ml) by initially encapsulating cells at 5×10^7 cells/ml within low fiber density (20%) fibrous assemblies (fig. S20). These high cell densities may be particularly useful in applications of the engineering of tissues and models for cell-dense tissues.

With regard to mechanical properties of fibrous assemblies with contraction, we observe that contracted constructs formed with low fiber densities (20%) have significantly higher compressive moduli (3.3 kPa) after 3 days when compared to constructs formed with higher fiber densities (1.4 and 1.8 kPa for 50 and 75%, respectively) (fig. S21, A and B). These results suggest that cells substantially stiffen assemblies with culture when compared to estimated noncontracted fibrous assembly moduli from rheological time sweeps as 0.006, 0.276, and 1.826 kPa for 20, 50, and 75% fibrous assemblies, respectively. ECM deposition also likely contributes to increased mechanics, as fibronectin is extensively deposited throughout contracted low fiber density constructs (20%), whereas fibronectin is limited to pericellular regions in higher fiber densities (fig. S21C). We observe that fibronectin production is similar across all fiber densities when fibronectin labeling is normalized to cell number. Thus, fiber density does not influence nascent ECM production, but contraction of low fiber density assemblies decreases the cell-to-cell distance and increases the extent of nascent ECM throughout the construct.

To further investigate cellular contributions to assembly stiffening with culture, we inhibit cell contraction with blebbistatin (myosin II inhibitor) or remove/lyse cells with SDS and observe that both of these perturbations result in decreased moduli, ~72 and 49% of nontreated gels, respectively (fig. S21D). Plastic deformation of the fibers can also influence mechanics, and low–cell density experiments with blebbistatin and SDS treatment do not result in recoiling of the fibers away from cells, suggesting that cells plastically deform fibrous assemblies (fig. S21E). These results further support the ECM-like properties of fibrous assemblies, showing that cells can stiffen assemblies and plastically deform them through contraction (*32*, *33*). Although cells embedded within fiber assemblies behave similarly to collagen, the differences in magnitude and kinetics still need to be explored further. These differences could be attributed to smaller fiber diameters, differences in the nature of interfiber crosslinks (*33*), supramolecular packing of collagen fibrils and fibers, cell-mediated crosslinking and/or degradation of collagen, biochemical ligands and presentation, and many other features of collagen that are not found in fiber assemblies (*10*).

Microtissues via contractile fibrous hydrogel assemblies

Microtissues formed from the cellular embedding and remodeling of ECM have been used to study cell and ECM organization during wound healing (*34*), model healthy and diseased tissue (*35*), and promote induced pluripotent stem cell maturation (*36*). This bottom-up approach relies on stromal cell ECM contraction and physical interactions with the matrix to form high–cell density tissue mimics (*3*). Although we have learned a great deal from current microtissue systems, there is a need for systems where the matrix can be tuned to better understand the contribution of ECM properties to tissue morphogenesis (*37*) and ECM-based diseases such as fibrosis (*38*). Currently, most commercially available ECM systems (e.g., type I collagen, fibrin, and Matrigel) have limited control over biochemical and biophysical properties and would benefit from synthetic versions where these properties can be modulated.

To address this need, we assess the potential for the fabrication of microtissues using fibrous assemblies, where cell contraction results in the formation of aligned tissues in the direction of principal stress dictated by micropost geometry (Fig. 5A). Micropost arrays with 1-, 2-, and 3-post geometries are fabricated to give tissues with cylindrical, uniaxial, and random alignment, respectively. Having observed extensive contraction with low fiber densities (20%), we use these formulations for microtissue formation. Microtissues form over 24 hours, resulting in circular-, dog bone–, and triangular-shaped tissues that can be cultured for 14 days to allow collagen I deposition with alignment that corresponds to macroscale tissue geometry (Fig. 5, B and C, and figs. S22 and S23). Specifically, 1-post geometries result in microtissues with circumferentially aligned collagen, 2-post geometries result in aligned collagen throughout the center of the microtissue, and 3-post geometries have randomly aligned collagen in the center of microtissues. NorHA fibers on the surface of microtissues align with the microtissue orientation, suggesting that fiber assemblies can be reorganized by cells to accompany their cell scale orientation (fig. S24); however, most of the fibers below the surface of aligned microtissues have an isotropic orientation. ECM alignment dictates cell shape and function, such as with circumferential alignment within arterial walls supporting dynamic changes in volumes, load-bearing tissues such as tendons needing highly aligned ECM, and glandular tissues such as the liver requiring isotropic ECM to support filtration. By introducing mechanical constraints, cells embedded within fiber assemblies transition from an initial isotropic orientation into organized tissues that mimic the ECM architecture found in some tissues. The 3D fibrous networks remain within the tissue after 14 days of culture, suggesting that these fibers not only facilitate but also integrate with the microtissue, which could be useful to provide further control over contracted microtissue differentiation and maturation (*39*).

Other synthetic materials that support microtissues have been described; however, these systems use either covalently crosslinked gels that require cell-mediated degradation that slows down tissue formation (*40*) or hydrogels crosslinked with dynamic covalent crosslinks that rapidly erode and limit control over material properties (*41*). Alternatively, fibrous assemblies provide a material system that promotes rapid tissue formation, and materials are integrated into the final tissue structure. The ease of tuning contractility should allow a broad range of cell types to be used across various emerging microtissue technologies (*39*). Beyond microtissue formation, fibrous assemblies could potentially be useful for other bottom-up approaches such as the self-assembly of vasculature (*2*), organoid culture and fusion (*42*), and microphysiological systems.

Programmable materials through extrusion printing and photopatterning

As the fibrous assemblies have many important features amenable to fabrication techniques, such as shear-thinning and self-healing behaviors and photocrosslinking, we explore their potential in contractile and dynamic constructs. Because of the extremely soft properties of fiber assemblies before photocrosslinking, we use an equally soft

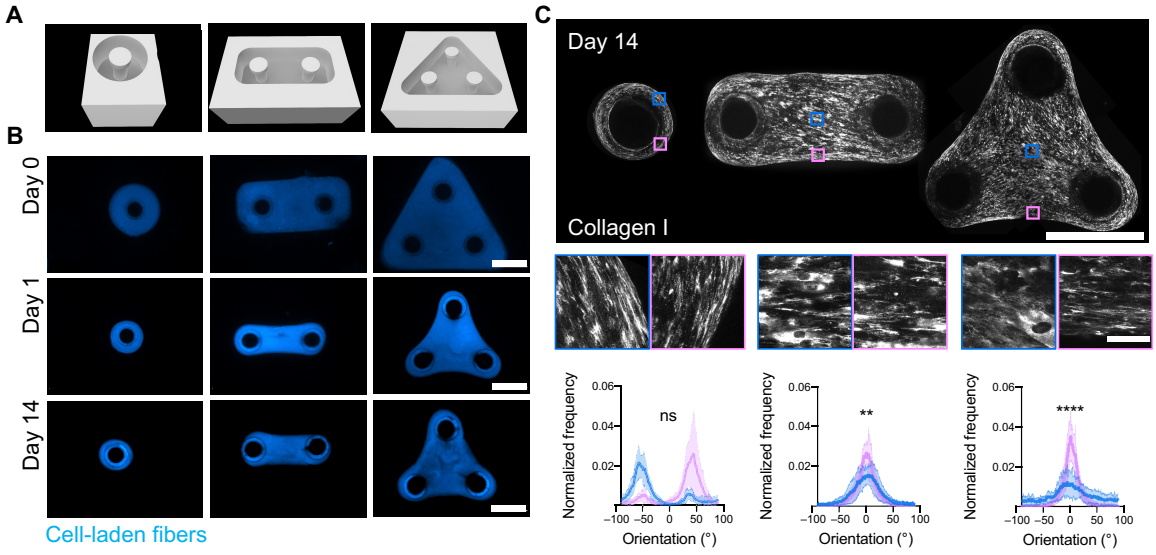

Fig. 5. Microtissue assembly and ECM organization in fibrous hydrogel assemblies. (**A**) Schematic of single, two, and three post microwells used to fabricate microtissues with circumferential, uniaxial, and random alignment, respectively. (**B**) MSC-laden NorHA fiber assemblies (20%, blue) formed in microwells and imaged at 0, 1, and 14 days. Images are representative of $n = 11$, 15, and 11 independent microtissues from three biologically independent experiments for single, two, and three post microwells, respectively. Scale bars, 2 mm. (**C**) Representative images of collagen I–labeled microtissues after 14 days of culture (top, macroscale images; scale bar, 1 mm; insets, highlights of color-coded regions; scale bar, 50 μm) and quantified collagen alignment profiles (bottom) from color-coded regions [$n = 11$, 15, and 11 independent microtissues from three biologically independent experiments for single, two, and three post microwells, respectively, mean ± SD, Watson-Wheeler test for homogeneity, two post (bottom center) $P = 0.0014$, three post (bottom right) $P = 6.4 \times 10^{-10}$] (**$P < 0.01$ and ****$P < 0.0001$).

($G' < 10$ Pa) support bath for the extrusion printing of low fiber density (20%) fiber solutions that would otherwise collapse if extruded onto a surface. Specifically, the support bath is composed of an agarose microgel slurry and unmodified HA, which allows yield stress properties and increased viscosity for handling, respectively (fig. S25). Cell-laden fibrous assemblies (75 and 20%) are extruded into the support bath, crosslinked with light, cultured for 24 hours, released from the support, and then imaged to assess changes in filament shape (Fig. 6A). High fiber density (75%) filaments do not contract, while low fiber density (20%) filaments contract down to ~46% of their original area and increase cell density (Fig. 6B), effectively increasing printing resolution.

Having shown that we can print contractile and noncontractile filaments, we next explore how the fusion of two filaments with differential contractility might contribute to geometric changes over time. Using multimaterial extrusion printing into support baths, contractile (low fiber density) and noncontractile (high fiber density) filaments are printed side by side and observed to undergo bending toward the direction of the contracting filament (Fig. 6C, left). Instabilities created by differential cell contraction are hypothesized to promote tissue bending during development and in engineered tissues (*8*, *43*), and our results suggest that fiber density can influence morphological changes in tissue shape. To further showcase the utility of this platform, we show that multiple bending instabilities can be introduced by printing multiple contractile filaments next to one larger noncontractile filament (Fig. 6C, right). These results indicate that the system is a highly tunable method to print tissues with predictable shape changes over time.

Photolithography-based printing methods are emerging as high-resolution alternatives to extrusion bioprinting with features around 10 to 100 μm (*44*); however, currently, there are no photocrosslinkable fibrous materials that are compatible with the requirements for photolithography-based printing, limiting the utility of these methods. Fibrous assemblies require photocrosslinking to stabilize fibers, making them ideal resins for photolithography-based printing. As a proof of concept, we use a digital micromirror device to create patterns of light to crosslink cell-laden fiber assemblies (Fig. 6D), and after photocrosslinking and washing, we obtain high-fidelity patterned structures (Fig. 6E and fig. S26). Star- and stick figure–shaped constructs are printed and allowed to contract overnight, and a high level of contraction is observed while retaining the original printed shape and simultaneously reaching tissue-level cell densities (Fig. 6E). To our knowledge, these are the first photocrosslinkable contractile bioinks that have been described, and they could find utility for fabricating constructs with tissue-relevant cell densities, high-resolution structures, and dynamic behaviors.

DISCUSSION

Advances in materials and processing techniques have enabled the development of hydrogels that capture many properties (e.g., structural, biochemical, and mechanical) of natural ECMs to mimic the complexity of native tissue environments to study cell-ECM interactions, enable the development of functional model systems, and engineer tissues. Many of these technologies rely on encapsulating cells within environments that lack the microscale structure and dynamic cell-responsive nature of the ECM, making it difficult for individual cells or collectives to undergo self-assembly processes that build the structures that give rise to tissue function. Fibrous assemblies allow cells to physically remodel their microenvironment to rapidly assemble organized microtissues while maintaining control over the microscale properties of the ECM. By modulating fibrous assembly porosity, cell-induced contractility of materials can be tuned and we demonstrate the potential for fabricating high–cell density

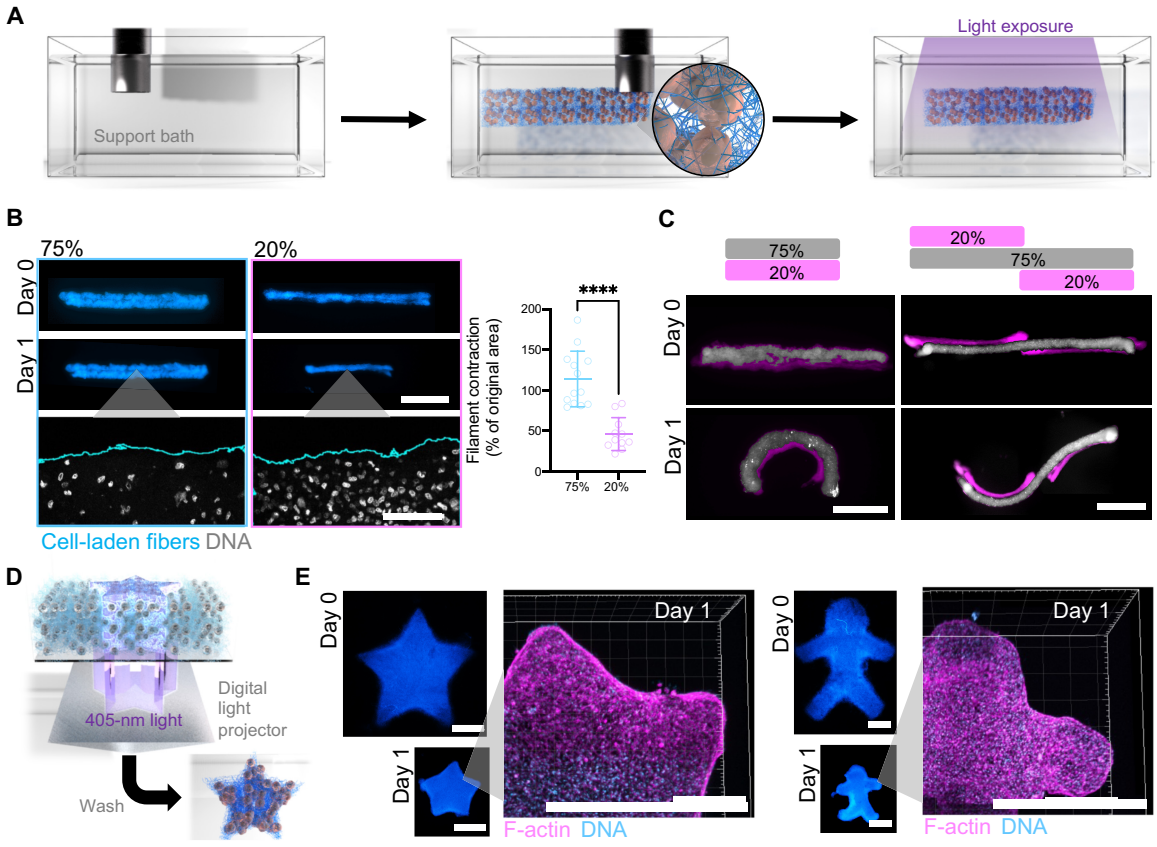

Fig. 6. Biofabrication of contractile and programmable cell-laden structures from fibrous hydrogel assemblies. (**A**) Schematic of extrusion bioprinting of cell-laden assemblies into support hydrogel bath and photocrosslinking into stabilized structures (right). (**B**) Representative images [top: scale bar, 1 mm; bottom: scale bar, 100 μm; filaments (blue), DNA (gray)] and quantification of bioprinted cell-laden filaments (NorHA assemblies) immediately (day 0) and after culture (day 1) ($n = 13$ and 11 individual filaments from three biological independent experiments for 75 and 20%, respectively; mean ± SD; two-tailed t test, $P = 9.0 \times 10^{-6}$). (**C**) Schematic (top) and representative images (bottom) of composite cell-laden filaments composed of 75% (gray) and 20% (pink) imaged immediately (day 0) and after culture (day 1). Images are representative of $n = 3$ (left, single bend) and $n = 2$ (right, multi-bend) biologically independent experiments each with two printed constructs. Scale bars, 1 mm (single bending, left) and 2 mm (multi-bend, right). (**D**) Schematic of projector-based photopatterning process (405-nm light), where structures are obtained with light-mediated patterning and washing of uncrosslinked fibers and cells. (**E**) Representative images of photopatterned star (left) and stick figure (right) structures contracting over 1 day and staining [actin (pink) and DNA (blue)] after 1 day of culture. Images are representative of three biologically independent experiments each. Scale bars, 1 mm (****$P < 0.0001$).

aligned microtissues. We believe this to be a substantial advance in the development of synthetic fibrous matrices to mimic natural ECM.

The potential application of fibrous assemblies in biofabrication techniques is explored by printing tissues that shrink to improve resolution and have programmable bending in 3D. A major goal in the biofabrication field is to create tissues that undergo morphological changes over time to mimic developmental processes or yield functional tissues (*44*–*46*). Our findings highlight how the microscale architecture and force-responsive properties of the ECM influence macroscopic changes in tissue shape over time and provide methods to program tissue bending. This was only possible through the development of new fibrous assemblies. Cell patterning (*43*), support gel fabrication (*5*), and high–cell density printing (*42*, *46*, *47*) are other emerging technologies to assemble tissues through cell-induced shape changes; however, most of these methods require natural ECMs that are permissive to cell interactions and function. Fibrous assemblies could be seamlessly integrated with these emerging methods to provide a high level of control over the microenvironment and assembly process. In addition, we believe that fibrous assemblies could enable developments in other areas, such as studying cell-ECM interactions (*48*), fabricating multi-tissue assembloids (*49*), or facilitating the integration of engineered tissue implants within hosts (*50*). The approach is highly generalizable and could be implemented with a wide range of materials and cell types, which opens up the exciting opportunity to direct self-assembly processes such as contraction, cell differentiation, and tissue morphogenesis over time.

Although we have demonstrated that fibrous assemblies recapitulate dynamic properties of natural ECM and the importance of fiber density on 3D cell contraction and macroscale morphological changes, there remain limitations to this study. There are endless formulations that can be fabricated with respect to material composition, which will influence network degradability and crosslink stability (e.g., covalent versus physical) and the extent to which the assemblies mimic natural ECM fibers (*10*); however, we have only selected a range of material formulations for this proof-of-concept illustration of the technique and potential utility of the approach. This includes the fabrication of fibrous assemblies of HA- and gelatin-based macromers, which illustrates some diversity in the system. We also provide some options for improving heterogeneity in material

structural properties; however, these could likely be further improved with emerging microfabrication methods (*51*). In addition, the impact of fiber density and length on contraction was the only material properties investigated here, and future work should explore how other parameters such as fiber stiffness and biochemical composition influence contractility and other outcomes. Last, MSCs were the only cells used in this study, and future work will need to explore the bioactivity of other cell types within these fibrous assemblies, particularly with specific applications in mind. For example, the behavior of endothelial cells, epithelial cells, and multicellular systems (spheroids or organoids) that undergo self-assembly processes would be of great interest.

MATERIALS AND METHODS

Polymer synthesis

All chemicals were purchased from MilliporeSigma unless noted otherwise. NorHA was synthesized as previously described (*52*). Briefly, sodium HA (Lifecore) was dissolved in Deionized (DI) H_2O at 2 wt % with Dowex resin (50Wx8 ion-change resin) at a ratio of 3:1 (resin:HA by weight) and mixed for at least 30 min. The resin was filtered, and the filtrate was titrated to pH 7.03 with diluted tetrabutylammonium hydroxide (TBA-OH) and then frozen and lyophilized. TBA modification of HA was confirmed with ^{1}H nuclear magnetic resonance (NMR). HA-TBA was dissolved in anhydrous dimethyl sulfoxide at 2 wt % with 4-(dimethylamino) pyridine (DMAP) (1.5 M ratio to HA-TBA repeat units) and 5-norbornene-2-carboxylic acid (3:1 M ratio to HA-TBA repeat units) under a nitrogen atmosphere. Once fully dissolved, di-tert-butyl dicarbonate (Boc_2O, 0.4 M ratio to HA-TBA units) was injected into the vessel and the reaction was carried out for ~20 hours at 45°C. The reaction was quenched with 2× cold (4°C) DI H_2O and dialyzed against water with 0.25 g of NaCl per liter of DI H_2O for 3 days. NorHA was then mixed with NaCl (1 g of NaCl/100-ml solution) and precipitated in ice-cold acetone (1 liter of acetone/100-ml solution). The precipitate was redissolved in DI H_2O, dialyzed for 5 days, frozen, and lyophilized. Norbornene functionalization was confirmed with ^{1}H NMR (fig. S1).

Norbornene-modified gelatin (NorGel) was synthesized as previously described (*53*). Briefly, 10 wt % gelatin was diluted in Dulbecco's phosphate buffered saline (DPBS) and heated to 60°C until fully dissolved, pH was adjusted to 7.5, 20 wt % carbic anhydride was added dropwise to the solution while stirring, and the reaction was carried out for 3 hours while maintaining pH ~8 with sodium hydroxide. The reaction was quenched using 5× volume of preheated DPBS, stirred for 15 min at 60°C, dialyzed at 40°C for 7 days, frozen, and lyophilized. Methacrylated HA (MeHA) was synthesized as previously described (*54*). Briefly, 2 g of HA was added to 200 ml of DI H_2O to achieve a 1 wt % solution of HA. Next, while maintaining a pH of 8.5 to 9, 1.5 ml of methacrylic anhydride was added dropwise and mixed on ice for 8 hours. The solution was mixed for an additional 12 hours at room temperature without maintaining pH, dialyzed for 7 days, frozen, and lyophilized. Norbornene-modified PEG (NorPEG; 8-arm PEG-Norbornene, 20 kDa) and thiol-modified PEG (4-arm PEG thiol, 5 kDa) were purchased from JenKem.

Electrospun fiber mat preparation

To electrospin NorHA, 3.5 wt % NorHA, 2.5 wt % PEO (900 kDa), 0.05% (v/v) Irgacure 2959, fluorescent dextran (4 mg/ml) [fluorescein isothiocyanate (FITC)–dextran, 2 MDa], and 1 mM RGD peptide (sequence: GCGYGRGDSPG) were mixed with various stoichiometric ratios of dithiothreitol (DTT) to norbornene groups (i.e., 0.1, 0.25, and 0.45 thiols:norbornenes) in DI H_2O, mixed at 250 rpm for 24 hours protected from light, and loaded into syringes for electrospinning. To electrospin NorGel, 5 wt % NorGel, 3.5 wt % PEO (900 kDa), 0.05% (v/v) Irgacure 2959, and fluorescent dextran (4 mg/ml; FITC-dextran, 2 MDa) were mixed with a 3.75 mM 4-arm PEG-thiol solution in DI H_2O. To electrospin NorPEG, 5 wt % 8-arm PEG-norbornene, 10 wt % 4-arm PEG-thiol, 2.5 wt % PEO (900 kDa), 0.05% (v/v) Irgacure 2959, and fluorescent dextran (4 mg/ml; FITC-dextran, 2 MDa) were mixed in DI H_2O. To electrospin MeHA, 3 wt % (MeHA), 2 wt % PEO (900 kDa), 0.05% (v/v) Irgacure 2959, and fluorescent dextran (4 mg/ml; FITC-dextran, 2 MDa) were mixed in DI H_2O. To electrospin GelMA, 10 wt % GelMA (~50% modification, Allevi), 0.05% (v/v) Irgacure 2959, and fluorescent gelatin (4 mg/ml; FITC-gelatin from pig skin, Thermo Fisher Scientific) were mixed in hexafluoro-2-propanol for 2 hours protected from light.

For single-polymer electrospinning, the electrospinning jet was positioned 19 cm away from a rotating collecting mandrel, where a flow rate of 0.7 ml/hour and a voltage of +28 to 30 kV were used. For multifiber electrospinning of stable (NorHA) and sacrificial (PEO) fiber populations, electrospinning jets were positioned on opposite sides of the electrospinning mandrel (fig. S5) while maintaining the same needle to collector distance (19 cm), and flow rates were modulated [1.05 ml/hour (PEO), 0.7 ml/hour (NorHA)] to give a 60:40 ratio of sacrificial to stable fibers within the fiber mat. Electrospinning was carried out in a custom humidity-controlled chamber (15 to 21% humidity) with a rotating mandrel (−5 kV, ~350 rpm) and needle gauge of 18. All fiber mats derived from norbornene-modified polymers were photocrosslinked for 1 hour on each side of the fiber mat surface at 10 mW/cm^2 with ultraviolet (UV) light (320 to 390 nm; OmniCure S1500 UV, Spot Cure Systems), while MeHA was photocrosslinked for 15 min on each side of the fiber mat surface at 15 mW/cm^2 with UV light. To photocrosslink GelMA, fiber mats were hydrated in 0.05 wt % I2959 dissolved in 100% ethanol for 10 min and then photocrosslinked in the hydrated state for 10 min at 10 mw/cm^2. Solution was rotated every 2.5 min to ensure equal light exposure. After crosslinking, ethanol was removed and fiber mats were hydrated with DPBS before fragmentation.

Cell isolation and culture

Human MSCs were isolated from bone marrow aspirate (Lonza) as previously described (*55*). Briefly, bone marrow was diluted with DPBS (1:4) and cells were separated with a Ficoll gradient (800*g* for 20 min). Mononuclear cells were isolated from the liquid interface, seeded on tissue culture plastic, and cultured in MSC expansion medium [α–minimum essential medium (MEM), 10% fetal bovine serum (FBS) (Gibco), 1% penicillin/streptomycin, and basic fibroblast growth factor (5 ng/ml)] at 37°C until reaching 80% confluency. Cells were then trypsinized and stored in liquid nitrogen. All MSCs were passaged one to three times in MSC culture medium (α-MEM, 10% FBS, and 1% penicillin/streptomycin), trypsinized using 0.05% trypsin/EDTA (Gibco), and resuspended in DPBS before encapsulation. All assemblies were cultured in MSC culture medium, and the medium was replaced every day.

Fiber fragmentation and purification

Eight milligrams of electrospun fiber mats was segmented (multiple ~2 mm by 2 mm squares) and hydrated with 6 ml of DPBS in a

sterile scintillation vial for 10 min, and then ~3 ml of the solution was repeatedly (40×) and rapidly aspirated and extruded through an 18-gauge needle (BD) in the same scintillation vial using a 3-ml syringe. A 21-gauge needle was then used to further fragment fibers with 40 repeated steps of aspiration and extrusion. Further fragmentation was achieved by using this same method with a 23-gauge needle, a 25-gauge needle, a 27-gauge needle, and finally a 30-gauge needle. Fiber solutions were purified by passing the solution sequentially through a 40-μm cell strainer (pluriSelect) and then a 5-μm cell strainer. Fibers were then pelleted with centrifugation at 10,000*g*, resuspended, and washed with 1 ml of phosphate-buffered saline, which was repeated twice to remove excess DTT crosslinker and I2959 photoinitiator. The fiber pellet volume was then measured by centrifuging, removing the supernatant completely, and resuspending in a known volume. The volume displaced by the pellet was taken as the volume of fibers at a 100% volume fraction. Fiber solutions were sterilized with germicidal UV and stored at 4°C.

Fiber assembly, NorHA hydrogel, and type I collagen hydrogel formation and cell encapsulation

Various concentrations of fibrous hydrogel assemblies (20, 50, and 75%, v/v) were formed by mixing the concentrated fiber solution with various amounts of PEG-thiol crosslinker (4-arm PEG thiol, 5 kDa) based on fiber volume concentration (0.1 mM for 20%, 0.25 mM for 50%, and 0.375 mM for 75%), 0.05 wt % photoinitiator (LAP), and Colorado Photopolymer Solutions (Boulder, CO) in DPBS. NorHA hydrogels were made by mixing 3.5 wt % NorHA polymer, 1 mM RGD, and 0.05 wt % LAP with stoichiometric ratios of DTT to norbornene groups (0.25. thiols:norbornenes) in DPBS. For cell encapsulation, these components were first mixed and cells were added last and kept on ice until use. Fibrous hydrogel assemblies and NorHA hydrogels were photocrosslinked using visible light (400 to 500 nm; OmniCure S1000) at an intensity of 5 mW/cm^2 for 5 min. Cell-laden constructs were carefully washed with cell culture medium immediately after crosslinking, and medium was changed 30 min later to remove any residual radicals and photoinitiator. Microfabricated polydimethylsiloxane (PDMS) (SYLGARD 184, DOW) wells (2 mm diameter) and 0.5-ml cut syringes were used as molds for low–cell density and high–cell density contraction assays, respectively.

Acid-solubilized type I bovine telocollagen (9.7 mg/ml, composed of 95% type I collagen and the remainder is type III collagen, Advanced BioMatrix) was mixed with acid-solubilized FITC-labeled type I bovine collagen (1 mg/ml; MilliporeSigma) to achieve a final stock concentration of 7.17 mg/ml (4 wt % FITC-labeled collagen, 96 wt % nonlabeled collagen, or 290 μl of labeled collagen with 710 μl of unlabeled collagen) and kept on ice for an hour before gel formation to ensure proper mixing. Collagen was mixed with prechilled 10× α-MEM and DPBS, and then 1 N NaOH was added to neutralize the collagen solution (typically: 0.023 ml × ml of collagen used = amount of 1 N NaOH to neutralize) to achieve a final concentration of 1, 2.5, or 6 mg/ml. Collagen was kept on ice until rheological characterization or cell suspensions were added. For rheological analysis, gels were polymerized for 20 min at 37°C on the rheometer. After cell suspensions were added, gels were polymerized for 20 min at 37°C in a 5% CO_2 incubator and then hydrated with cell culture medium.

Material and cell imaging analysis

To measure fiber lengths, a custom FIJI macro was written to binarize fluorescent images of dilute fiber solutions, and ridge detector was used to measure fiber lengths. Fiber diameter and porosity were measured using previously described methods (*54*). Void fractions of fibrous hydrogel assemblies were measured by thresholding fluorescent images of assemblies, inverting the images, and measuring the % area of the signal. This gives the void fraction for an *xy* plane by measuring the area of the pores, and this measurement was used to measure the average void fraction for 10 slices through ~10 μm in the *z* direction.

Cell shape descriptors were obtained from max *z* projections of phalloidin and Hoechst 33342–stained cells. Images were binarized, and aspect ratios and cell circularity were measured using FIJI. To measure fiber compaction around cells, a region of interest was created around cells on a single *xy* plane near the *z* position of the cell nucleus, and fiber fluorescence intensity was measured in 1-μm band increments away from the cell border (fig. S8). Fiber fluorescence intensity around cells was compared to a remote location without cells and normalized by the average fluorescence intensity (+ SD) for remote locations. Cell viability was measured by casting assemblies in wells at initial time points or by sectioning gels with a scalpel and staining with Hoechst 33342 (5 μg/ml; stains all cell nuclei, Fisher Scientific) and ethidium homodimer-1 (4 μM; stains dead cell nuclei, Invitrogen) for later time points.

Macroscale contraction of assemblies was measured by manually segmenting and measuring the construct area from phase-contrast images over time. Volumetric changes were obtained by measuring the height and circumference of contracted assemblies after 3 days of culture using phase-contrast microscopy. Contraction of microtissues, extrusion printed constructs, and photopatterned constructs were imaged with fluorescence and bright-field microscopy.

Rheological and mechanical characterization

The viscoelastic, photocrosslinking, and stiffening properties of fiber solutions, fibrous hydrogel assemblies, and support hydrogels were characterized using shear rheology [cone and plate geometry with (0.995°) cone angle and a 27-μm gap or parallel plate geometry, TA Instruments, AR2000] at room temperature or at 37°C for collagen gels. To assess the shear-thinning properties, the storage modulus (G') and viscosity were measured as a function of strain (0.005 to 5) and shear rate (0 to 50/s), respectively. Photocrosslinking of fibrous hydrogel assemblies was measured in real time at low strain (0.01) at 1 Hz. To assess strain-induced stiffening properties, G' was measured at a function of increasing strain (0.005 to 1) at 1 Hz. Self-healing of fiber solutions and support gels was assessed by applying low (0.01) and high (5) strains repeatedly at 1 Hz. The compressive moduli of contracted assemblies were measured using dynamic mechanical analysis (TA Instruments, Q800).

Microwell fabrication, microtissue formation, and photopatterning

Microwell hydrogels with various post geometries were fabricated using a DLP printer (Volumetric, Lumen X) with PEG-diacrylate resin (PEGDA PhotoInk), and MSC-laden fiber solutions were seeded into microwells with a 20-μl pipette and then crosslinked with light. Microtissues were then hydrated with MSC culture medium, and the medium was changed 30 min later and every day after for 14 days.

To photopattern cell-laden structures, custom PDMS wells were fabricated and cell-laden fiber solutions were added to the well. The DLP printer was used to project various photopatterns (i.e., star and stick figure) that photocrosslinked the fibrous hydrogel assemblies

along the light path and created stable 3D structures. A light intensity of 20 mW/cm^2 (405-nm light-emitting diode) for 30 s was used to create photopatterned constructs. After photopatterning, constructs were gently hydrated with small droplets of MSC culture medium near the edge of the print and then flooded with excess medium. Constructs were imaged immediately after washing and after 1 day of contraction.

Support gel preparation and extrusion bioprinting

Agarose support gels were made as previously described (*56*), with some modifications. Briefly, a 0.5 wt % agarose (SeaKem, Lonza) solution was mixed and autoclaved to melt and sterilize and then cooled while stirring at 700 rpm to form microgels. This microgel solution was then diluted in an 8 wt % solution of HA to give a final agarose concentration of 0.25 wt % and HA concentration of 4 wt %. Agarose was diluted to give a support gel that was soft enough to yield with extremely soft fiber solutions. HA was added to diluted agarose microgel solution to increase the viscosity and stabilize the printed structures while moving. Fiber solutions were extruded using 27-gauge needles and a submicroliter injection needle (World Precision Instruments, Nano-Fil 100), with two different extrusion printers (Allevi 2 and Velleman K8200), and photocrosslinked (400 to 500 nm, 5 mW/cm^2 for 5 min) after printing. Filaments were imaged directly after printing and after releasing prints from the support bath at ~20 hours of culture by diluting with an equal volume of MSC medium.

Immunofluorescent labeling and staining

After terminal time points, cultures were fixed with prewarmed 4% paraformaldehyde for 30 min and then washed with 3× DPBS. Large constructs used in macroscale contraction assays were fixed overnight at 4°C, cryoprotected in 30% sucrose solution, embedded in optimal cutting temperature compound, flash-frozen by dipping into liquid nitrogen–cooled 2-methyl butane, and cryosectioned (20-μm sections). Actin and DNA were visualized by staining with Alexa Fluor 647 phalloidin (Cell Signaling Technology) and Hoechst 33342 (Fisher Scientific). For immunolabeling, sections or microtissues were hydrated, blocked with 1% bovine serum albumin (BSA) in DPBS for 1 hour at room temperature, and then incubated with either anti-fibronectin (1:50; Sigma-Aldrich F6140) or anti–collagen type I (1:200; Abcam ab138492) in 1% BSA buffer overnight at 4°C. The next day, sections and microtissues were washed three times with DPBS and then incubated with the secondary antibodies Alexa Fluor 647 anti-mouse (1:200; A-21235, Fisher Scientific) and Alexa Fluor 594 anti-goat (ab150080) for 2 hours at room temperature and then counterstained with Hoechst 33342. Sections and microtissues were imaged using a Leica SP5 confocal microscope.

Fiber network model

Three-dimensional discrete Voronoi fiber networks were used to model the networks (*31*). To generate a Voronoi network, first, random seed points were chosen in a 3D domain. The Voronoi diagram corresponding to these seed points was then generated using MATLAB (MathWorks, Natick, MA). Beam elements and modeling fibers were considered along the edges of the resulting Voronoi diagram. To perform mechanical tests, we extracted a cubic sample from the constructed network. The fibers were curved to mimic the experimental images and facilitate the computations. Individual fibers were modeled as elastic rods with circular sections, capable of bending, stretching, and shear. Hybrid beam formulation and reduced integration were used to facilitate computations. The fiber elastic modulus was 1 MPa.

In this model, the dimensionless ratio of fiber diameter to Voronoi cell diameter controls the network's deformation. The variations of network density were modeled using fiber–to–cell diameter ratios of about 1, 4, and 6%, which were obtained by iteration through various fiber–to–cell diameter ratios until these network densities matched the experimental data with 20, 50, and 75% fibrous hydrogel assemblies, respectively. The mean connectivity (nodal coordination) of the network model is between 3 and 4 to match the experimentally observed network connectively. Displacement-controlled tests were performed by prescribing the displacement of boundary nodes. Shear tests were performed by fixing the displacement of the nodes at the bottom surface of the network while horizontally moving the nodes at the top surface. In addition, the networks were stretched in uniaxial tests while free to contract in the directions transverse to loading. Implicit finite element calculations were performed using the ABAQUS software package (Simulia).

Statistical analysis

Microsoft Excel was used to store raw data, while GraphPad Prism 9 was used for all statistical analysis. Comparisons between two experimental groups were performed using two-tailed *t* tests, and comparisons among more groups were performed using a one-way analysis of variance (ANOVA) with Tukey post hoc testing or multiple groups over time using either a two-way ANOVA with Tukey post hoc test or a mixed-effects analysis with Sídák post hoc testing. Circular statistics were performed using the package "circular" in R software, where Watson-Wheeler test for homogeneity was carried out on two different groups (*57*). All *n* numbers refer to biologically independent samples with no repeated measures, and *P* values are provided in figure legends. The sample distributions were assumed to be normal with equal variance.

SUPPLEMENTARY MATERIALS

Supplementary material for this article is available at https://science.org/doi/10.1126/sciadv.abi8157

REFERENCES AND NOTES

1. P. Ngo, P. Ramalingam, J. A. Phillips, G. T. Furuta, Collagen gel contraction assay. *Methods Mol. Biol.* **341**, 103–109 (2006).
2. H.-H. G. Song, R. T. Rumma, C. K. Ozaki, E. R. Edelman, C. S. Chen, Vascular tissue engineering: Progress, challenges, and clinical promise. *Cell Stem Cell* **22**, 340–354 (2018).
3. W. R. Legant, A. Pathak, M. T. Yang, V. S. Deshpande, R. M. McMeeking, C. S. Chen, Microfabricated tissue gauges to measure and manipulate forces from 3D microtissues. *Proc. Natl. Acad. Sci. U.S.A.* **106**, 10097–10102 (2009).
4. A. Lee, A. R. Hudson, D. J. Shiwarski, J. W. Tashman, T. J. Hinton, S. Yerneni, J. M. Bliley, P. G. Campbell, A. W. Feinberg, 3D bioprinting of collagen to rebuild components of the human heart. *Science* **365**, 482–487 (2019).
5. C. D. Morley, S. T. Ellison, T. Bhattacharjee, C. S. O'Bryan, Y. Zhang, K. F. Smith, C. P. Kabb, M. Sebastian, G. L. Moore, K. D. Schulze, S. Niemi, W. G. Sawyer, D. D. Tran, D. A. Mitchell, B. S. Sumerlin, C. T. Flores, T. E. Angelini, Quantitative characterization of 3D bioprinted structural elements under cell generated forces. *Nat. Commun.* **10**, 3029 (2019).
6. M. A. Skylar-Scott, S. G. M. Uzel, L. L. Nam, J. H. Ahrens, R. L. Truby, S. Damaraju, J. A. Lewis, Biomanufacturing of organ-specific tissues with high cellular density and embedded vascular channels. *Sci. Adv.* **5**, eaaw2459 (2019).
7. S. R. Caliari, J. A. Burdick, A practical guide to hydrogels for cell culture. *Nat. Protoc.* **13**, 405–414 (2016).
8. J. M. Jaslove, C. M. Nelson, Smooth muscle: A stiff sculptor of epithelial shapes. *Philos. Trans. R. Soc. Lond. B Biol. Sci.* **373**, 20170318 (2018).
9. M. D. Davidson, J. A. Burdick, R. G. Wells, Engineered biomaterial platforms to study fibrosis. *Adv. Healthc. Mater.* **9**, 1901682 (2020).

10. F. Burla, Y. Mulla, B. E. Vos, A. Aufderhorst-Roberts, G. H. Koenderink, From mechanical resilience to active material properties in biopolymer networks. *Nat. Rev. Phys.* **1**, 249–263 (2019).
11. C. Storm, J. J. Pastore, F. C. MacKintosh, T. C. Lubensky, P. A. Janmey, Nonlinear elasticity in biological gels. *Nature* **435**, 191–194 (2005).
12. H. Wang, A. S. Abhilash, C. S. Chen, R. G. Wells, V. B. Shenoy, Long-range force transmission in fibrous matrices enabled by tension-driven alignment of fibers. *Biophys. J.* **107**, 2592–2603 (2014).
13. E. A. Aisenbrey, W. L. Murphy, Synthetic alternatives to Matrigel. *Nat. Rev. Mater.* **5**, 539–551 (2020).
14. E. Prince, E. Kumacheva, Design and applications of man-made biomimetic fibrillar hydrogels. *Nat. Rev. Mater.* **4**, 99–115 (2019).
15. R. K. Das, V. Gocheva, R. Hammink, O. F. Zouani, A. E. Rowan, Stress-stiffening-mediated stem-cell commitment switch in soft responsive hydrogels. *Nat. Mater.* **15**, 318–325 (2015).
16. D. C. Schoenmakers, A. E. Rowan, P. H. J. Kouwer, Crosslinking of fibrous hydrogels. *Nat. Commun.* **9**, 1–8 (2018).
17. M. Wang, C. Cui, M. M. Ibrahim, B. Han, Q. Li, M. Pacifici, J. T. R. Lawrence, L. Han, L. H. Han, Regulating mechanotransduction in three dimensions using sub-cellular scale, crosslinkable fibers of controlled diameter, stiffness, and alignment. *Adv. Funct. Mater.* **29**, 1808967 (2019).
18. B. M. Baker, B. Trappmann, W. Y. Wang, M. S. Sakar, I. L. Kim, V. B. Shenoy, J. A. Burdick, C. S. Chen, Cell-mediated fibre recruitment drives extracellular matrix mechanosensing in engineered fibrillar microenvironments. *Nat. Mater.* **14**, 1262–1268 (2015).
19. B. Kessel, M. Lee, A. Bonato, Y. Tinguely, E. Tosoratti, M. Zenobi-Wong, 3D bioprinting of macroporous materials based on entangled hydrogel microstrands. *Adv. Sci.* **7**, 2001419 (2020).
20. L. H. Han, X. Tong, F. Yang, Photo-crosslinkable PEG-based microribbons for forming 3D macroporous scaffolds with decoupled niche properties. *Adv. Mater.* **26**, 1757–1762 (2014).
21. D. L. Matera, W. Y. Wang, M. R. Smith, A. Shikanov, B. M. Baker, Fiber density modulates cell spreading in 3D interstitial matrix mimetics. *ACS Biomater Sci. Eng.* **5**, 2965–2975 (2019).
22. B. Miller, A. Hansrisuk, C. B. Highley, S. R. Caliari, Guest–host supramolecular assembly of injectable hydrogel nanofibers for cell encapsulation. *ACS Biomater Sci. Eng.* **7**, 4164–4174 (2021).
23. M. D. Davidson, E. Ban, A. C. M. Schoonen, M.-H. Lee, M. D'Este, V. B. Shenoy, J. A. Burdick, Mechanochemical adhesion and plasticity in multifiber hydrogel networks. *Adv. Mater.* **32**, 1905719 (2020).
24. B. M. Baker, A. O. Gee, R. B. Metter, A. S. Nathan, R. A. Marklein, J. A. Burdick, R. L. Mauck, The potential to improve cell infiltration in composite fiber-aligned electrospun scaffolds by the selective removal of sacrificial fibers. *Biomaterials* **29**, 2348–2358 (2008).
25. A. D. Doyle, N. Carvajal, A. Jin, K. Matsumoto, K. M. Yamada, Local 3D matrix microenvironment regulates cell migration through spatiotemporal dynamics of contractility-dependent adhesions. *Nat. Commun.* **6**, 8720 (2015).
26. A. Omidinia-Anarkoli, S. Boesveld, U. Tuvshindorj, J. C. Rose, T. Haraszti, L. De Laporte, An injectable hybrid hydrogel with oriented short fibers induces unidirectional growth of functional nerve cells. *Small* **13**, 1702207 (2017).
27. T. G. Kim, T. G. Park, Biodegradable polymer nanocylinders fabricated by transverse fragmentation of electrospun nanofibers through aminolysis. *Macromol. Rapid Commun.* **29**, 1231–1236 (2008).
28. M. S. Hall, F. Alisafaei, E. Ban, X. Feng, C.-Y. Hui, V. B. Shenoy, M. Wu, Fibrous nonlinear elasticity enables positive mechanical feedback between cells and ECMs. *Proc. Natl. Acad. Sci. U.S.A.* **113**, 14043–14048 (2016).
29. W. R. Legant, J. S. Miller, B. L. Blakely, D. M. Cohen, G. M. Genin, C. S. Chen, Measurement of mechanical tractions exerted by cells in three-dimensional matrices. *Nat. Methods* **7**, 969–971 (2010).
30. C. D. Davidson, D. K. P. Jayco, W. Y. Wang, A. Shikanov, B. M. Baker, Fiber crimp confers matrix mechanical nonlinearity, regulates endothelial cell mechanosensing, and promotes microvascular network formation. *J. Biomech. Eng.* **142**, 111009 (2020).
31. E. Ban, H. Wang, J. M. Franklin, J. T. Liphardt, P. A. Janmey, V. B. Shenoy, Strong triaxial coupling and anomalous Poisson effect in collagen networks. *Proc. Natl. Acad. Sci. U.S.A.* **116**, 6790–6799 (2019).
32. Y. L. Han, P. Ronceray, G. Xu, A. Malandrino, R. D. Kamm, M. Lenz, C. P. Broedersz, M. Guo, Cell contraction induces long-ranged stress stiffening in the extracellular matrix. *Proc. Natl. Acad. Sci. U.S.A.* **115**, 4075–4080 (2018).
33. E. Ban, J. M. Franklin, S. Nam, L. R. Smith, H. Wang, R. G. Wells, O. Chaudhuri, J. T. Liphardt, V. B. Shenoy, Mechanisms of plastic deformation in collagen networks induced by cellular forces. *Biophys. J.* **114**, 450–461 (2018).
34. M. Selman Sakar, J. Eyckmans, R. Pieters, D. Eberli, B. J. Nelson, C. S. Chen, Cellular forces and matrix assembly coordinate fibrous tissue repair. *Nat. Commun.* **7**, 11036 (2016).
35. K. T. Wagner, T. R. Nash, B. Liu, G. Vunjak-Novakovic, M. Radisic, Extracellular vesicles in cardiac regeneration: Potential applications for tissues-on-a-chip. *Trends Biotechnol.* **39**, 755–773 (2020).
36. K. Ronaldson-Bouchard, S. P. Ma, K. Yeager, T. Chen, L. J. Song, D. Sirabella, K. Morikawa, D. Teles, M. Yazawa, G. Vunjak-Novakovic, Advanced maturation of human cardiac tissue grown from pluripotent stem cells. *Nature* **556**, 239–243 (2018).
37. Y. Zhao, N. Rafatian, E. Y. Wang, N. T. Feric, B. F. L. Lai, E. J. Knee-Walden, P. H. Backx, M. Radisic, Engineering microenvironment for human cardiac tissue assembly in heart-on-a-chip platform. *Matrix Biol.* **85–86**, 189–204 (2020).
38. D. Chen, L. R. Smith, G. Khandekar, P. Patel, C. K. Yu, K. Zhang, C. S. Chen, L. Han, R. G. Wells, Distinct effects of different matrix proteoglycans on collagen fibrillogenesis and cell-mediated collagen reorganization. *Sci. Rep.* **10**, 19065 (2020).
39. M. J. Mondrinos, F. Alisafaei, A. Y. Yi, H. Ahmadzadeh, I. Lee, C. Blundell, J. Seo, M. Osborn, T. J. Jeon, S. M. Kim, V. B. Shenoy, D. Huh, Surface-directed engineering of tissue anisotropy in microphysiological models of musculoskeletal tissue. *Sci. Adv.* **7**, eabe9446 (2021).
40. J. Liu, K. Miller, X. Ma, S. Dewan, N. Lawrence, G. Whang, P. Chung, A. D. McCulloch, S. Chen, Direct 3D bioprinting of cardiac micro-tissues mimicking native myocardium. *Biomaterials* **256**, 120204 (2020).
41. Z. Wei, R. Schnellmann, H. C. Pruitt, S. Gerecht, Hydrogel network dynamics regulate vascular morphogenesis. *Cell Stem Cell* **27**, 798–812.e6 (2020).
42. J. A. Brassard, M. Nikolaev, T. Hübscher, M. Hofer, M. P. Lutolf, Recapitulating macro-scale tissue self-organization through organoid bioprinting. *Nat. Mater.* **20**, 22–29 (2021).
43. J. M. Viola, C. M. Porter, A. Gupta, M. Alibekova, L. S. Prahl, A. J. Hughes, Guiding cell network assembly using shape-morphing hydrogels. *Adv. Mater.* **32**, 2002195 (2020).
44. A. C. Daly, M. E. Prendergast, A. J. Hughes, J. A. Burdick, Bioprinting for the biologist. *Cell* **184**, 18–32 (2021).
45. A. Ding, O. Jeon, R. Tang, Y. Bin Lee, S. J. Lee, E. Alsberg, Cell-laden multiple-step and reversible 4D hydrogel actuators to mimic dynamic tissue morphogenesis. *Adv. Sci.* **8**, 2004616 (2021).
46. K. T. Lawlor, J. M. Vanslambrouck, J. W. Higgins, A. Chambon, K. Bishard, D. Arndt, P. X. Er, S. B. Wilson, S. E. Howden, K. S. Tan, F. Li, L. J. Hale, B. Shepherd, S. Pentoney, S. C. Presnell, A. E. Chen, M. H. Little, Cellular extrusion bioprinting improves kidney organoid reproducibility and conformation. *Nat. Mater.* **20**, 260–271 (2021).
47. O. Jeon, Y. Bin Lee, H. Jeong, S. J. Lee, D. Wells, E. Alsberg, Individual cell-only bioink and photocurable supporting medium for 3D printing and generation of engineered tissues with complex geometries. *Mater. Horiz.* **6**, 1625–1631 (2019).
48. V. A. Patil, K. S. Masters, Engineered collagen matrices. *Bioengineering* **7**, 163 (2020).
49. N. Vogt, Assembloids. *Nat. Methods* **18**, 27 (2021).
50. K. R. Stevens, M. A. Scull, V. Ramanan, C. L. Fortin, R. R. Chaturvedi, K. A. Knouse, J. W. Xiao, C. Fung, T. Mirabella, A. X. Chen, M. G. McCue, M. T. Yang, H. E. Fleming, K. Chung, Y. P. De Jong, C. S. Chen, C. M. Rice, S. N. Bhatia, In situ expansion of engineered human liver tissue in a mouse model of chronic liver disease. *Sci. Transl. Med.* **9**, eaah5505 (2017).
51. A. J. D. Krüger, O. Bakirman, L. P. B. Guerzoni, A. Jans, D. B. Gehlen, D. Rommel, T. Haraszti, A. J. C. Kuehne, L. De Laporte, Compartmentalized jet polymerization as a high-resolution process to continuously produce anisometric microgel rods with adjustable size and stiffness. *Adv. Mater.* **31**, 1903668 (2019).
52. W. M. Gramlich, I. L. Kim, J. A. Burdick, Synthesis and orthogonal photopatterning of hyaluronic acid hydrogels with thiol-norbornene chemistry. *Biomaterials* **34**, 9803–9811 (2013).
53. Z. Mũnoz, H. Shih, C. C. Lin, Gelatin hydrogels formed by orthogonal thiol-norbornene photochemistry for cell encapsulation. *Biomater. Sci.* **2**, 1063–1072 (2014).
54. M. D. Davidson, K. H. Song, M.-H. Lee, J. Llewellyn, Y. Du, B. M. Baker, R. G. Wells, J. A. Burdick, Engineered fibrous networks to investigate the influence of fiber mechanics on myofibroblast differentiation. *ACS Biomater Sci. Eng.* **5**, 3899–3908 (2019).
55. O. F. W. Gardner, M. Alini, M. J. Stoddart, Mesenchymal stem cells derived from human bone marrow. *Methods Mol. Biol.* **1340**, 41–52 (2015).
56. B. B. Mendes, M. Gómez-Florit, A. G. Hamilton, M. S. Detamore, R. M. A. Domingues, R. L. Reis, M. E. Gomes, Human platelet lysate-based nanocomposite bioink for bioprinting hierarchical fibrillar structures. *Biofabrication* **12**, 015012 (2020).
57. U. Lund, C. Agostinelli, H. Arai, A. Gagliardi, E. Garcia Portuges, D. Giunchi, J.-O. Irisson, M. Pocermnich, F. Rotolo, Package "circular" (2017); www.topsoe.com/processes/sng.
58. S. M. Mitchell, S. Lange, H. Brus, Gendered citation patterns in international relations journals. *Int. Stud. Perspect.* **14**, 485–492 (2013).
59. J. D. Dworkin, K. A. Linn, E. G. Teich, P. Zurn, R. T. Shinohara, D. S. Bassett, The extent and drivers of gender imbalance in neuroscience reference lists. *Nat. Neurosci.* **23**, 918–926 (2020).
60. D. Maliniak, R. Powers, B. F. Walter, The gender citation gap in international relations. *Int. Organ.* **67**, 889–922 (2013).

Acknowledgments: We acknowledge C. Loebel, K. H. Song, L. Wang, and V. Muir for help and advice with MSC isolation and culture, polymer synthesis, material fabrication, and NMR spectroscopy, respectively. **Funding:** This work was supported by the National Science Foundation through the Center for Engineering MechanoBiology STC (CMMI-1548571) and the UPenn MRSEC program (DMR-1720530), as well as through the NIH (F32 DK117568 to M.D.D. and R01AR056624 to J.A.B.). **Author contributions:** M.D.D. and J.A.B. conceived the ideas and designed the experiments. M.D.D., M.E.P., E.B., K.L.X., G.M., P.M., and A.D. conducted experiments and computational studies and interpreted the data. M.D.D. and J.A.B. wrote the manuscript. M.D.D., M.E.P., E.B., K.L.X., G.M., P.M., A.D., P.A.J., V.B.S., and J.A.B. interpreted the data and edited the manuscript. All authors have given approval to the final version of the manuscript. **Competing interests:** The authors declare that they have no competing interests.

Data and materials availability: All data needed to evaluate the conclusions in the paper are present in the paper and/or the Supplementary Materials. **Citation diversity statement:** Recent work in several fields of science has identified a bias in citation practices such that papers from women and other minority scholars are undercited relative to the number of papers in the field (*58*–*60*). We recognize this bias and have worked diligently to ensure that we are referencing appropriate papers with fair gender and racial author inclusion.

Submitted 2 April 2021
Accepted 20 September 2021
Published 10 November 2021
10.1126/sciadv.abi8157